Considerations on scaling behavior in avalanche flow: Implementation in a simple mass block model

Peter Gauer

Norwegian Geotechnical Institute, P.O. Box 3930, Ullevål Stadion, NO–0806, Oslo, Norway

ABSTRACT

Observations of runout distances combined with velocity measurements suggest that "major" dry-mixed avalanches show a scale invariance to the total drop height H_{SC}. This is in accordance to the proposed upper-limit envelope of the maximum velocity by McClung and Schaerer (2006). The observations are also supported by a simple scaling analysis using a simple mass block model on cycloidal and parabolic tracks (Gauer, 2018b), concluding $U_{max} \sim \sqrt{gH_{SC}/2}$. In this supplementary paper, a simple mass block model is presented that includes basic observations of major dry-mixed avalanches, such as mass entrainment and deposition, and that reflects this scale invariance. Almost all model parameters can principally be observed in the field. Model results are compared with a series of avalanche observations of runout and velocity and match well, considering that the model is a first order approximation.

1. Introduction

Snow avalanches are severe threats to the population and their infrastructure in many snow covered areas, typically in mountainous regions, but also in regions that have only small relief (< 100 m) (e.g. Issler et al., 2016; Hetu et al., 2011). Delineation of avalanche endangered areas or the design of sufficient mitigation measures require in-depth understanding on the avalanche phenomenon. Practitioners are mostly interested in expected runout distances, velocity distributions along the track, and for some purposes flow heights.

In (Gauer, 2018b), the author tried to derive the principle scaling behavior of major (dry-mixed) avalanches by simply considering the behavior of a mass block along cycloidal and parabolic tracks. Comparing the results with runout observations and velocity measurements suggested that the maximum velocity scales as $U_{max} \sim \sqrt{gH_{SC}/2}$ and that the mean retarding acceleration dependence on the mean slope angle. However, the author did not specify the form of the retarding acceleration in more detail. In this supplementary paper, a simple mass block model is presented that combines a series of recent avalanche observations and measurements and reflects the observed scaling behavior. Mass block models have long been proposed, e.g. (Voellmy, 1964; Perla et al., 1980; Norem et al., 1987), but their proposed parameter choices fail to reproduce the observed scaling behavior. For a discussion on the scale dependency of Voellmy-type models and the NIS model see Gauer (2014).

The following section gives a brief summary of observations relevant for the model framework. It is followed by a section introducing the governing equations of the mass block model that incorporates these observations. In Section 4 various model results are presented. To demonstrate the model performance, model results are compared qualitatively with avalanche measurements of runout and front-velocity. Thereby, a more descriptive or exploratory statistics approach is used; focus of this paper is not a detailed calibration of the model. In Section 5 some limitations and outlooks are given. In this paper, we focus mainly on dense or fluidized dry-mixed avalanches but disregard the accompanying powder (suspension) part. This distinction is not always done in field observations, which can cause some uncertainty in their interpretation.

2. Observations

In this section, avalanche observations are presented that are relevant for avalanche models and can provide constraints for relevant parameter values. These observations constitute the framework for the present model.

Lied and Bakkehøi (1980) were the first to propose a relation between the path geometry and the observed runout distance of "major" avalanches (i.e. avalanches of relative size $\geq R4$, cf. Greene et al., 2016). Many of their avalanches have probably returns periods of the order of 100 years and can be considered as rare events, but not necessarily as the most extreme ones. Lied and Bakkehøi expressed the runout by the ratio between vertical drop and horizontal runout distance, $\tan\alpha = H/L$. Based on several hundred avalanche observations,

they developed the so-called $\alpha - \beta$ model for Norway, whereby the most extreme α-angle observed in a given path is related to the mean steepness of this path. The mean steepness is approximated by the slope angle β of the line connecting the upper boundary of release area and the point in the track where the terrain gradient falls below 10°. The proposed final relation does not include any length scale, suggesting a scale invariance or more specific an invariance to a change in drop height. The proposed relation implies also that any other length scales involved can only occur as constant ratios or within a dimensionless parameter. The model was later adapted in many other countries. The background data of the model provide a valuable data set and despite the variety of the data sets, the tendency in the various countries is very similar. Fig. 1 a shows a collection of observed runout angles α versus the corresponding β-angle. For more information on those data see Gauer et al. (2010) and references therein. The figure shows also the estimated exceedance probability of α versus β according to the $\alpha - \beta$ model.

McClung and Schaerer (2006) suggested, mainly based on data from Rogers Pass (BC), that the relation $U_{max} = 1.8\sqrt{H_{SC}}$ provides an upper-limit envelope for the maximum velocity in an avalanche path, where H_{SC} is the total vertical drop height. Fig. 1 b shows the Complementary Cumulative Distribution Function (CCDF, survivor function) of
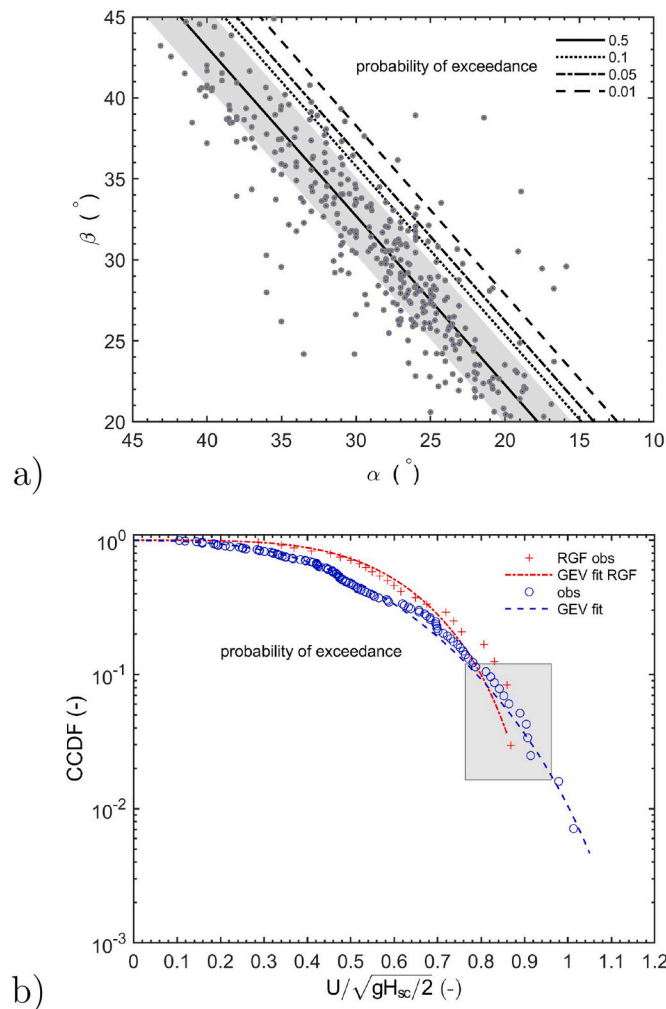
observed values of the scaled maximum velocity $U_{max}/\sqrt{gH_{SC}/2}$ at Ryggfonn and for avalanches from various other locations (for more information on those data see McClung and Gauer, 2018). g is the gravitational acceleration.

Gauer (2013, 2014) investigated a series avalanche observations from various test-sites for which velocity data along the track or at least for a major part of it are available. He suggested that the velocity of major (dry-mixed) avalanches scales as $U_{max} \sim (0.5 - 0.7)\sqrt{gH_{SC}}$. A summary of the measured velocity data from Ryggfonn (NO) is included in the later Fig. 7. Similarly, Fig. 8 includes a comparison for several "major" avalanches from various other locations covering a range of $H_{SC} \approx [120\ \text{m}, 1200\ \text{m}]$ (for information on those avalanches see Gauer, 2013, 2014, and the references therein). Based on these measurements, Gauer (2014) concluded that the proposed scaling behavior has implications for the choice of the empirical parameters for avalanche models, which use a velocity dependent friction law with fixed parameters. He argued that the measurements suggest a lower explicit velocity dependency of the bed friction than generally proposed. His suggestion is in line with back-calculations by Ancey and Meunier (2004).

Little hard data on typical release masses or fracture depths of major avalanches is published; a little more is reported on estimated deposition volumes. Fig. 2 presents a collection of observed deposition volumes related to the drop height of the avalanches. The relation suggests larger deposition volumes are observed in larger tracks. The power law dependency is in accordance with observations by McClung (2009), but can also partly be attributed to entrainment along the track.

Gauer and Issler (2004) and Sovilla (2004) emphasized the importance of mass entrainment long the avalanche track. Gauer and Issler noted that erosion and entrainment of mass can contribute considerably to the retardation of an avalanche. They estimated a ratio between the contribution due to entrainment and due to frictional losses of the order of 0.2. Even if an avalanche does not entrain all the available snow, ploughing through an intact snowpack will cause a resistance on the avalanche. Gauer (2016) presented estimations on the averaged erosion depth for Ryggfonn and compared those with estimates from other locations. At Ryggfonn, avalanches entrained on average approximately 0.25 m snow along the track, whereas the mean entrainment depth for the other observations is about 0.4 m. This higher value might be expected as these avalanches are regarded more extreme events on average. The estimates are in accordance with measurements presented by Sovilla et al. (2006). Hence, entrainment
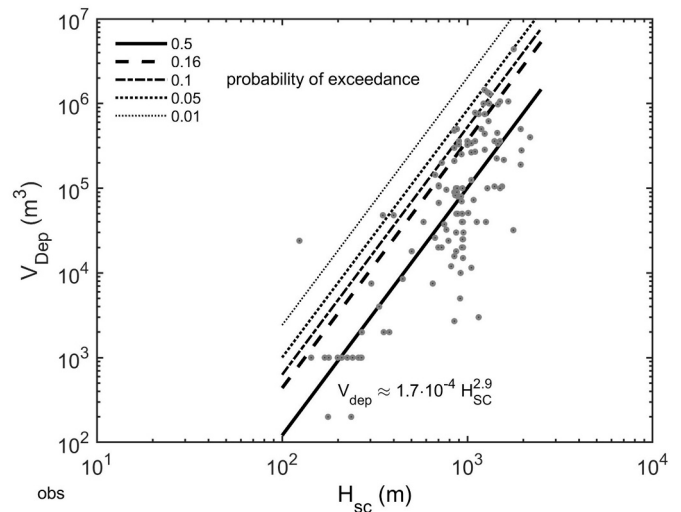

a)

b)

Fig. 1. a) Runout observations and estimated exceedance probabilities of α versus β according to the $\alpha - \beta$ model ($\alpha_m = 0.96\beta - 1.4°$; gray shaded area $\pm \sigma$; for explanation see Lied and Bakkehøi, 1980). b) Complementary Cumulative Distribution Function (CCDF, survivor function) of observed values of $U_{max}/\sqrt{gH_{sc}/2}$ at Ryggfonn and avalanches at various locations. The gray rectangle indicates a region that covers typical "major" events (c.f. Fig. 8).

Fig. 2. Observed avalanche deposit volumes of "major avalanche events" versus total drop height H_{SC} (for references to the data see Gauer et al., 2010). The lines show the estimated exceedance probabilities derived from these observations.
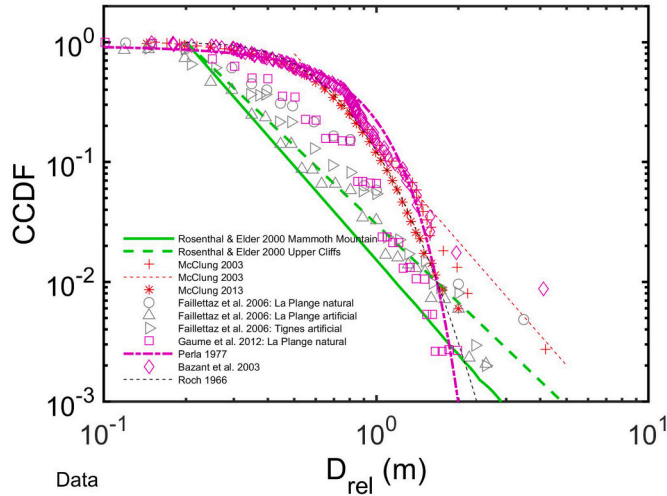
Fig. 3. Complementary cumulative distribution function of the fracture depth D_{rel}; observations or proposed relations in the literature.

plays an important role in the mass balance, which is indicated by Fig. 2.

On the other hand, observations by Sovilla et al. (2010) indicate that avalanches may begin to deposit—mainly starting from the tail—at a slope angle of approximately 30°, which is in the range of typical friction angles for snow on snow (Lang and Dent, 1982; van Herwijnen and Heierli, 2009).

Both processes, entrainment and deposition, are important for the mass balances of an avalanche and therefore for its dynamics.

As far as the fracture height is concerned, Fig. 3 shows a comparison of the complementary cumulative distribution function (survival function) of observed fracture depths D_{rel} and proposed relations in the literature (Rosenthal and Elder, 2003; McClung, 2003; Perla, 1977; Faillettaz et al., 2006; Gaume et al., 2012; Bazant et al., 2003). The comparison suggests that values between 1 and 2 m could be considered rare (i.e. have probabilities in the range of 0.01 and 0.1). There is however a considerable spread in the data and the observational data might be biased to minor events.

Dry-mixed avalanches can be considered as granular flows consisting of small snow clouds with sizes typically less than 0.1 m, where the dissipation is considered to be dominated by a Coulomb-type friction with an effective friction factor $\tan\delta_e$ (e.g. Coaz, 1910; Savage and Hutter, 1989). Savage and Hutter proposed an ansatz

$$\tan\delta_e = \frac{p_{xz}(\nu, \dot{\gamma})}{p_{zz}(\nu, \dot{\gamma})} \tag{1}$$

where p_{xz} is the shear stress, p_{zz} the normal stress, ν the solids fraction, and $\dot{\gamma}^2 = (du/dz)^2$ is the shear rate squared. For a free surface flow, Savage and Hutter argued that in the limit of very small shear rates Eq. (1) reduces to

$$\tan\delta_e = \tan\delta_s(\nu) \tag{2}$$

δ_s is termed the quasi-static friction angle. For high shear rates they argued that Eq. (1) tends to

$$\tan\delta_e = \tan\delta_D(\nu) \tag{3}$$

where $\delta_D(\nu)$ is the dynamic friction angle which, based on experiments, was suggested to be fairly close to δ_s. They further mentioned that experiments showed very little rate-dependence in the stress ratio and that experiments suggested that the standard deviations of the stress ratios was approximately 10% of the mean for a given material. Savage and Hutter advocated that both the interior and the basal friction angles are rate independent.

A shear-rate independence is in accordance with the observations on runout and maximum velocity for major dry-mixed avalanches—both are governed by the total drop height. Effects due to varying flow heights, where the flow height is a second length scale, should only be of second-order at most.

3. Governing equations

In this section, we formulate the governing equations for a simple sliding block model (center of mass model) with varying mass. The model includes basic observations of major dry-mixed avalanches, such as mass entrainment and deposition, and reflects the observed scale invariance to changes in drop height. Almost all model parameters can be traced back to field observations. A similar model was proposed, e.g., by Cherepanov and Esparragoza (2008); Cherepanov (2019). However, in our case, we also allow for mass loss and we disregard the explicit velocity squared dependent resistance term (often referred to as 'turbulent' velocity-dependent resistance), which is included in most present-days avalanche models. The 'turbulent' velocity-dependent resistance introduces a scale dependency that is in this way not observed in the measurements. On the other hand, we retain implicit terms that dependent on the velocity such as the effect of curvature or terms arising from a varying mass.

The governing equation for the mass balance is

$$\frac{dM}{dt} = (\rho_s d_e - \rho_a d_d)\frac{ds}{dt} \tag{4}$$

where the avalanche mass per unit width $M = \rho_a V$ with the density of the flowing avalanche ρ_a and V its volume per unit width. The density of the intact snowpack along the track is ρ_s and $d_e(s)$ is the depth of snow measured perpendicular to the track that is entrained by the avalanche and $\rho_a d_d(s)$ is the mass loss due to deposition. The traveled distance (arc-length) along the avalanche track at time t is $s(t)$.

The momentum of the sliding block will change due to entrainment and deposition of mass. Let us recall the principle of linear momentum, which states that the momentum $L_{(t+\Delta t)}$ at time $t + \Delta t$ of a system (in our case the system of the avalanche, entrained snowpack and deposited mass) is equal to the sum of the momentum of the system L_t at time t and the impulse $\int_t^{(t+\Delta t)} R\,dt$ of the resultant of all forces acting on the system:

$$L_{(t+\Delta t)} = L_t + \int_t^{(t+\Delta t)} R\,dt \tag{5}$$

Now, the linear momentum of the avalanche and the mass entrained by the avalanche, ΔM_e, at time t, shortly before ΔM_e is entrained, is just the sum of both,

$$L_t = (MU)_t + (\Delta M_e U_e)_t \tag{6}$$

where U is the velocity of the avalanche and U_e the velocity of the mass ΔM_e. After ΔM_e is entrained and ΔM_d has separated (deposited) from the avalanche, the new avalanche mass $M + \Delta M_e - \Delta M_d$ moves at the same velocity $U + \Delta U$. The momentum of the system is now

$$\begin{aligned} L_{(t+\Delta t)} &= (M + \Delta M_e - \Delta M_d)(U + \Delta U) + \Delta M_d U \\ &= MU + (\Delta M_e - \Delta M_d)U + M\Delta U + (\Delta M_e - \Delta M_d)\Delta U + \Delta M_d U \end{aligned} \tag{7}$$

$\Delta M_d U$ is the momentum of the deposited mass separated from the avalanche. Using Eqs. (7) and (6) in (5), we obtain

$$M\Delta U + (\Delta M_e - \Delta M_d)U + \Delta M_d U = \Delta M_e U_e + \int_t^{(t+\Delta t)} R\,dt \tag{8}$$

After rearranging and dividing by Δt, one gains

$$M\frac{\Delta U}{\Delta t} + \frac{(\Delta M_e - \Delta M_d)}{\Delta t}U$$
$$= \frac{1}{\Delta t}\int_t^{(t+\Delta t)} R\,dt + \frac{\Delta M_e}{\Delta t}U_e - \frac{\Delta M_d}{\Delta t}U - \frac{(\Delta M_e - \Delta M_d)\Delta U}{\Delta t} \tag{9}$$

which becomes in the limit $\Delta t \to 0$

$$M\frac{dU}{dt} + \frac{dM}{dt}U = R + Q_e U_e - Q_d U \tag{10}$$

Here, we use $\lim_{\Delta t \to 0}(\Delta M_e - \Delta M_d)/\Delta t = dM/dt$ and assume $\lim_{\Delta t \to 0}(\Delta M_e - \Delta M_d)\Delta U/\Delta t = 0$. The mass fluxes are $dM_e/dt = Q_e$ and $dM_d/dt = Q_d$. With $U(s) = ds/dt$ and $\Lambda(s) \equiv [M(s)U(s)]^2$ and by using Eq. (4), Eq. (10) can be rewritten as

$$\frac{d\Lambda}{ds} = 2M(s)\left(R\left[s, \frac{\sqrt{\Lambda}}{M(s)}\right] - \rho_a d_d \frac{\Lambda}{M(s)^2} + \rho_s d_e \frac{\sqrt{\Lambda}\,U_e}{M(s)}\right) \tag{11}$$

For a known resulting force $R\left[s, \frac{\sqrt{\Lambda}}{M(s)}\right]$, Eq. (11) can be integrated numerically and the avalanche speed $U(s)$ found as function of s:

$$U(s) = \frac{1}{M(s)}\sqrt{2\int_0^s M(s)R_{eff}\left[s, \frac{\sqrt{\Lambda}}{M(s)}\right]ds + (U_0 M_0)^2} \tag{12}$$

where the effective resulting force is

$$R_{eff} = R\left[s, \frac{\sqrt{\Lambda}}{M(s)}\right] - \rho_a d_d \frac{\Lambda}{M(s)^2} + \rho_s d_e \frac{\sqrt{\Lambda}\,U_e}{M(s)} \tag{13}$$

The avalanche mass $M(s)$ follows from Eq. (4)

$$M(s) = \int_0^s (\rho_s d_e - \rho_a d_d)ds + M_0 \tag{14}$$

The initial conditions are $s = 0$, $U(0) = U_0$, $M(0) = M_0$, and in the case of entrainment from rest $U_e = 0$. If one includes particle impacts and rebouncing (i.e. saltation), U_e will be larger than zero. For signs of saltation see, e.g., (Gauer et al., 2008, Fig. 13), but for now we disregard particle saltation. In the following, we use the ansatz

$$R\left[s, \frac{\sqrt{\Lambda}}{M(s)}\right] = M(s)(g\sin\phi - a_0\max\left(0, g\cos\phi + \kappa\frac{\Lambda}{M(s)^2}\right)) - K_e\sqrt{2d_e} \tag{15}$$

for the resulting force on the avalanche, where ϕ is the local slope angle, g the gravitational acceleration, $a_0(= \tan\delta_{be})$ is the effective coefficient of friction in which δ_{be} is the basal friction angle. κ is the local curvature of the track. The last term on the right hand side expresses the fracture resistance of the snowpack, where K_e is the so-called entrainment toughness (cf. Cherepanov, 2019; Cherepanov and Esparragoza, 2008).

Now using

$$\frac{dM}{ds} = \rho_s d_e - \rho_a d_d \tag{16}$$

and

$$\frac{d\Lambda}{ds} = 2M(s)\left(\frac{dM}{ds}U(s)^2 + M(s)U(s)\frac{dU}{ds}\right) \tag{17}$$

the equation of motion is written as

$$M(s)U(s)\frac{dU}{ds} = R[s, U(s)] - \rho_a d_d U(s)^2 + \rho_s d_e U(s)U_e - \frac{dM}{ds}U(s)^2 \tag{18}$$

or by using Eq. (16) as

$$M(s)U(s)\frac{dU}{ds} = R[s, U(s)] + \rho_s d_e(U(s)U_e - U(s)^2) \tag{19}$$

For $dU/ds = 0$ and $U_e \approx 0$ and ansatz (15), an equation for the

maximum velocity is found:

$$U_m(s_m) = \sqrt{\frac{g\left(\sin\phi_m - a_0\cos\phi_m - \frac{K_e\sqrt{2d_e}}{gM(s_m)}\right)}{\left(a_0\kappa(s_m) + \frac{\rho_s d_e}{M(s_m)}\right)}} \tag{20}$$

where the subscript $(\cdot)_m$ marks the point where the maximum velocity is reached.

Now, on parabolic or cycloidal tracks, the curvature can be given as $\kappa = c(\varsigma, \phi_0)/H_{SC}$, where H_{SC} is the total drop height of the path, ς is the scaled travel distance, and ϕ_0 is the initial slope angle. According to (14), it is furthermore reasonable to assume that the avalanche mass can be approximated as $M(s) \approx m(\varsigma)H_{SC}$. For example, assuming an initial mass M_0 per meter width

$$M_0 \approx \rho_r D_{rel}\frac{c_0 H_{SC}}{\sin\phi_0} \tag{21}$$

where, ρ_r is the averaged density of the snowpack in the release area, D_{rel} is the fracture depth and c_0 a coefficient describing the length of the release area relative to the length of the track (i.e. $c_0 H_{SC}/sin\phi_0$ is the slope parallel length of the release area l_{rel}). Typically, c_0 might be in the range of 0.1 to 0.3, that is the height difference of in release area is about 10 to 30% of the total drop height H_{SC}. If we now consider a cycloid, the mass can be written as

$$M(s) = m(\varsigma)H_{SC} = M_0\left(1 + \frac{2(\rho_s d_e - \rho_a d_d)}{c_0\rho_r D_{rel}}\frac{(\sin\phi_0 - \sin\phi_1(\varsigma))}{\sin\phi_0}\right) \tag{22}$$

where $\phi_1(\varsigma)$ is the slope angle along the track. Hence, the dimensionless maximum velocity, $\mathbb{U}_m \equiv U/\sqrt{gH_{SC}}$, can be written as

$$\mathbb{U}_m = \sqrt{\frac{\left(\sin\phi_m - a_0\cos\phi_m - \frac{K_e\sqrt{2d_e}}{gH_{SC}m(\varsigma_m)}\right)}{a_0 c(\varsigma_m, \phi_0) + \frac{\rho_s d_e}{m(\varsigma_m)}}} \tag{23}$$

For $K_e\sqrt{2d_e} \ll gH_{SC}m(\varsigma)$, $\mathbb{U}_m$ is nearly independent of the total drop height of the track, which is in accordance to the observations on major avalanches (cf. Gauer, 2014, 2013, 2018b; McClung and Gauer, 2018). For a cycloid, $c(\varsigma, \phi_0)$ increases with increasing ϕ_0 and decrease with increasing ς. For parabolic tracks, there is an increase with increasing ς at first, and an increase for ϕ_0. The increase with slope angle compensates partly the effect of the slope angle dependency of the Coulomb-friction term and contributes to a more constant retarding acceleration along the track. In addition, the increase in total mass causes a reduction of the velocity depending term, which is caused by mass entrainment itself. This counterbalances the increasing Coulomb-friction in the lower part of the track. Mass deposition counteracts the reduction due to entrainment. These feedback mechanisms lead to a rather constant apparent retarding accelerations (i.e. the sum of frictional contribution and due to entrainment) for major avalanches, which is in concert with energy considerations for observations by Gauer (2013).

Eq. 23 implies also that the ratio between snow entrainment and initial mass ($\rho_s d_e/c_0\rho_r D_f$) has a decisive role for fast moving avalanches and long runouts. A smaller ratio favors higher velocities.

To account for the drag due to the quiet ambient air, let us assume a resistance term which is proportional to the area of the interface and the square of the avalanche velocity. Eq. (15) becomes

$$R\left[s, \frac{\sqrt{\Lambda}}{M(s)}\right] = M(s)(g\sin\phi - a_0\max\left(0, g\cos\phi + \kappa\frac{\Lambda}{M(s)^2}\right)) - \frac{\rho_{air}c_{Da}l_a}{M(s)}\frac{\Lambda}{M(s)^2} - K_e\sqrt{2d_e} \tag{24}$$

where ρ_{air} is the density of air and l_a is the length of the avalanche. In this case, Eq. 23 rewrites to

$$\mathbb{U}_m = \sqrt{\frac{\left(\sin\phi_m - a_0\cos\phi_m - \frac{K_e\sqrt{2d_e}}{g\,H_{SC}\,m(\varsigma_m)}\right)}{a_0 c(\varsigma_m,\phi_0) + \frac{\rho_s d_e + c_{Da}\rho_{air}l_a}{m(\varsigma_m)}}} \tag{25}$$

In a first estimate, one may assume $l_a \sim l_{rel}$. As long as $\rho_s d_e \gg \rho_{air}c_{Da}l_a$, the drag due to the ambient air can safely be neglected. Otherwise, the air drag might introduce a dependency on the total drop height through l_a. As a conservative estimate, the drag coefficient c_{Da} is assumed to be in the order of 0.01 (see for example Curcic and Haus, 2020).

Recalling that for major dry snow avalanches $\mathbb{U}_m$ will typically be larger than $0.75/\sqrt{2}$ but probably not much larger than $1.1/\sqrt{2}$. In this case, Eq. (25) provides some constraints on the parameter values and for contributions due to possible further terms that might have been neglected here.

4. Model test

The following section presents several comparisons between observations and model calculations. We do not try to provide a detailed parameter calibration, rather we use first estimates on the parameters based on the observations presented in Sec. 2 to demonstrate the general model performance. Thereby, we primarily consider major dry-mixed avalanches (i.e. relative size $\geq$ R4). Hence, the parameter choice might be biased in regard to those observations.

4.1. Parameters

All parameters, except of the effective friction parameter a_0 and the drag coefficient c_{Da}, can in principle be observed in the field. For the effective basal friction parameter, a_0, we choose as a first estimate

$$a_0 \approx 0.3. \tag{26}$$

This corresponds to an effective basal friction angle of $\delta_{be} \approx 17°$. The value is, e.g., in agreement with measurements by Platzer et al. (2007) for dry snow, which were done on a chute. Also Heimgartner (1977) found similar values. As previously indicated, the exact value of a_0 may to a certain degree depend on the state of flow and properties of the avalanche, like flow density, clod size, humidity, and other. It actually may vary to a certain degree along the track. However, this is outside of the scope of the present paper.

Observations of erosion depth at Ryggfonn, mentioned above, show typical erosion depths in the range of 0.1 m to 0.4 m with a median of around 0.25 m (Gauer and Kristensen, 2016). Estimates based on a series major avalanches in various tracks show a similar range, but a somewhat higher mean (Gauer, 2016). These estimates are in accordance with measurements by Sovilla et al. (2006). In the simulations, we use

$$d_e(s) = H_e \cos\phi(s) \tag{27}$$

where H_e is the erosion depth measured vertically.

For the entrainment toughness K_e in Eq. (15), we follow the ansatz for the fracture toughness by Schweizer et al. (2004):

$$K_e = A_c \left(\frac{\rho_s}{\rho_{ice}}\right)^{B_c} \tag{28}$$

The density of ice is $\rho_{ice} \approx 917$ kg m^{-3}. Lacking better data at present, we assume $A_c \approx 8$ kPa$\sqrt{m}$ and $B_c \approx 2.3$. For cases of our concern, $K_e\sqrt{2d_e}/g\,H_{SC}\,m(\varsigma)$ is typically less than 0.01 and the effect can be neglected for a first order approximation.

Observations by Sovilla et al. (2010) suggest that avalanches start to deposit at slope angles of approximately 30°, which is in the range of typical friction angles for snow (cf. Lang and Dent, 1982; van Herwijnen and Heierli, 2009). Here, due to lack of better knowledge, we use a simple approach to include mass loss. We assume
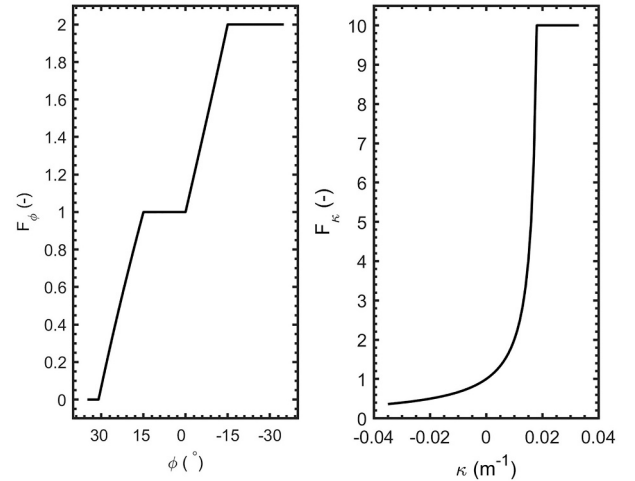

Fig. 4. Factors F_ϕ and F_κ for the deposition model. Here with $\mu_d = \tan(15°)$.

$$d_d(s) = d_{d0}F_\phi F_\kappa \tag{29}$$

where d_{d0} is a parameter and $F_{\phi(s)}$ and $F_{\kappa(s)}$ are functions of the slope angle and curvature, respectively.

$$F_\phi = \min\left(1, \max\left(0, \frac{\mu_s - \tan(\phi(s))}{\mu_s - \mu_d}\right)\right) + \min\left(1, \max\left(0, 1 - \frac{\tan(\phi(s))}{\tan(15°)}\right)\right) \tag{30}$$

where $\mu_s (\approx 0.6)$ is the friction coefficient for snow on snow, μ_d is an additional parameter regulating the intensity. In a first approximation, we assume $d_{d0} = d_e(s)\rho_s/\rho_a$ and $\mu_d = 0$. This implies that the avalanche will gain mass as long as $d_e > 0$ and $\phi > 0$. This may not be the case for all avalanches, especially for minor ones where the mass balance might become negative. A dependency on the curvature is also included by

$$F_\kappa = \frac{1}{\max\left(0.1, 1 - \frac{\kappa(s)}{\kappa_m}\right)} \tag{31}$$

where κ_m is set to 0.02 m^{-1}. This implies less tendency to deposit on convex slopes but a drastic increase of deposition on very concave slopes. Fig. 4 shows a plot of both factors.

Calculations with a simple release model (Gauer, 2018a) suggest that the expected fracture depth decreases with increasing slope angle of the release zone and can be approximated by

$$D_{rel} \approx HS_0 \cos\phi_0 \tag{32}$$

where HS_0 is an appropriated snow depth for an avalanche release. Observations on fracture depths are shown in Fig. 3, which suggest $HS_0 \sim 2$ m as a first estimate for major avalanches.

Table 1 gives a summary of the first guess parameter values used in the following sections, if not otherwise stated.

4.2. Parabolic and cycloidal tracks

In the first test, we follow the proposed approach in Gauer (2018b) and study tracks with a simple geometry. The simulations are carried out for cycloidal and parabolic tracks with varying mean steepness, which is approximated by the β-angle. Fig. 5 shows the runout simulations using the parameter values given in Table 1. The runout is expressed by the runout angle α. For comparison, observed α-angles are shown and the relation of the $\alpha - \beta$ model for the mean α_m angle

$$\alpha_m = b_1\beta + b_0 \tag{33}$$

In the Norwegian version, $b_1 = 0.96$ and $b_0 = -1.4°$. The gray shaded area shows the corresponding $\pm \sigma$-range. For the simulations,

Table 1
Estimates on typical parameter values.

Parameter	ρ_r	ρ_s	ρ_a	HS_0	c_0	H_e	a_0	μ_s	μ_d	c_{Da}
Unit	[kg m^{-3}]	[kg m^{-3}]	[kg m^{-3}]	[m]	[−]	[m]	[−]	[−]	[−]	[−]
	200	150	150	2	0.15	0.5	0.3	0.6	0	0.01
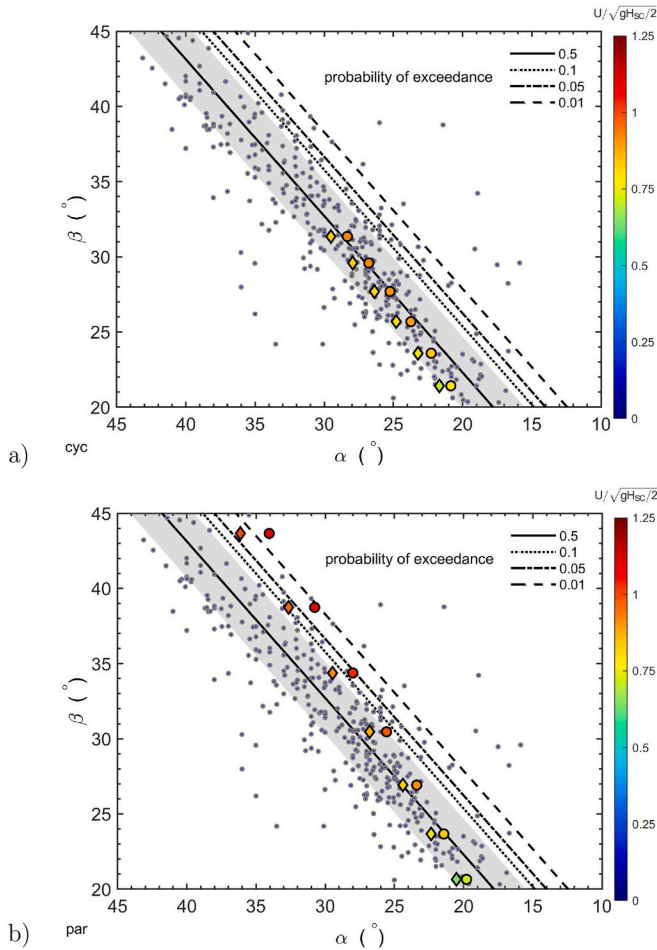
Fig. 5. Simulated runout marked by the α-angle and maximum velocity (color coded) on a) cycloidal and b) parabolic tracks with the mean slope angle, β, as parameter. (•) marks runs with $H_e = 0.25$ m and (♦) those with $H_e = 0.5$ m. The remaining parameters are given in Table 1. Observations are shown as gray dots.

$H_e = 0.25$ m and $H_e = 0.5$ m are used. On the cycloidal track, the model follows the expected trend in Eq. (33) very well. For the parabolic track, the simulations suggest a slightly less steep trend ($b_1 \approx 0.65$). Still, the overall trend is reflected. By the way, a less steep curve is actually purposed for avalanches in Colorado ($b_1 = 0.63$) and Nevada ($b_1 = 0.67$)(cf. Gauer, 2018b, and references therein). The maximum velocity for the simulations is as expected, with $U/\sqrt{gH_{SC}/2} \sim 0.8$ on the cycloidal and $U/\sqrt{gH_{SC}/2} \sim 0.9$ on the parabolic track. This difference may be traced back to the difference in the overall curvature for cycloidal and parabolic tracks.

The figure shows also the effect of different erosion rates with otherwise unchanged parameters—higher mass intake along the track causes higher retardation resulting in lower maximum velocities and shorter runouts.

The simulations are carried out for a total drop height $H_{SC} = 1000$ m, however, as the model is invariant to H_{SC}, simulations with other drop heights show no differences. That the model behaves invariant to
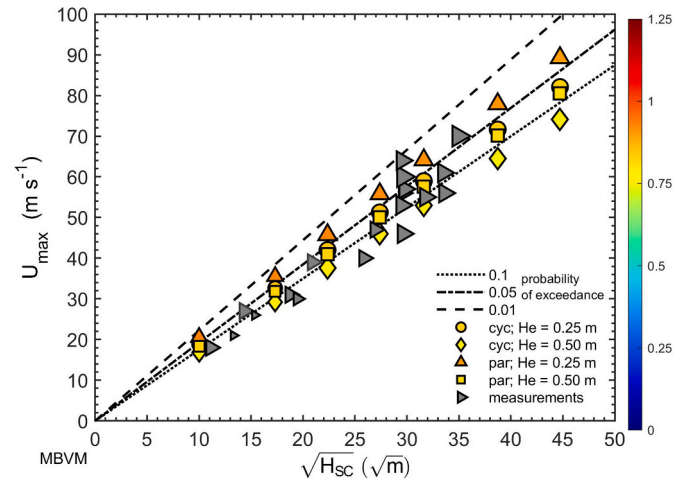

Fig. 6. Simulated maximum velocity, U_{max}, versus square root of the drop height, $\sqrt{H_{SC}}$. The color illustrates the scaled velocity $U_{SC} = U_{max}/\sqrt{gH_{SC}/2}$. The lines show the estimated exceedance probabilities derived from observations shown in Fig. 3. The figure shows example calculations for a cycloidal and parabolic track and two erosion depths. The initial slope angle ϕ_0 of the tracks is 40°. The remaining parameters are given in Table 1. The gray triangles depict measured maximum front-velocities from major avalanche events in various tracks (c.f. Fig. 8). The lines depict the probability of exceedance in Fig. 1 b.

H_{SC} is demonstrated in Fig. 6, which shows $U_{max} \propto \sqrt{H_{SC}}$. The figure shows example calculations for a cycloidal and parabolic track with an initial slope angle $\phi_0 = 40°$ and $H_e = 0.5$ m and $H_e = 0.25$ m. The lines depict the probability of exceedance according to Fig. 1 b. For comparison, the measured maximum front velocity for a series of major avalanche events (c.f. Fig. 8) are presented too. The simulations capture the observed trend well.

4.3. Ryggfonn (NO)

Fig. 7 shows a comparison of a series of avalanche observations at the Norwegian avalanche test-site Ryggfonn (for more details on the data see, e.g. Gauer and Kristensen, 2016) and a simulation with a slightly adapted parameter set. In accordance with the observations $M_0 \approx 5 \cdot 10^4$ kg m^{-1} and $H_e = 0.25$ m is used. The remaining parameters are given in Table 1. The simulation provides a good first estimate on the larger events observed at the test-site.

4.4. Major events

Fig. 8 illustrates the comparison of measured front-velocities from major avalanche events in various tracks with the mass block calculations. For details on the measurements, see (Gauer, 2014, 2013, 2018b). To facilitate a comparison, the path geometries are scaled by the drop height H_{SC} and the velocity as $U/\sqrt{gH_{SC}/2}$. As in the case for the Ryggfonn simulation, the model provides a reasonable good first estimate for those major events, both in respect to runout and velocity. As proposed, the apparent retarding acceleration is rather constant and the ratio between losses due to entrainment and frictional losses varies between approximately 0–0.3 along the track with a mean of ≈ 0.17.
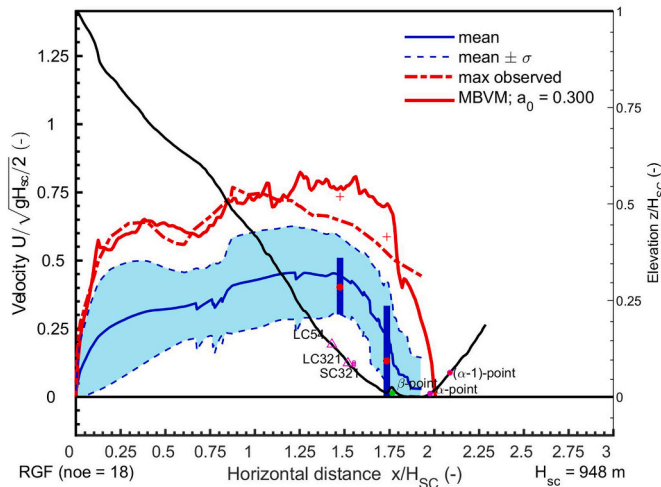
Fig. 7. Simulation (red solid line) for the Ryggfonn path (Norway). The main parameters are given in Table 1, however, in accordance with the observations $M_0 \approx 5 \cdot 10^4$ kg m^{-1} and $H_e = 0.25$ m is used. For comparison, the range of observed front velocities along the track at the Ryggfonn-site is given. The blue line shows the mean, the shaded area the $\pm \sigma$-range and the red dashed line shows the observed maximum derived from observations along the track. In addition, bars show the interquartile range of the front velocity U_{LC} measured between load plates LC54 and LC321 and the front velocity U_b at the base of the catching dam. The red dots show the corresponding means and red crosses mark the measured maxima.
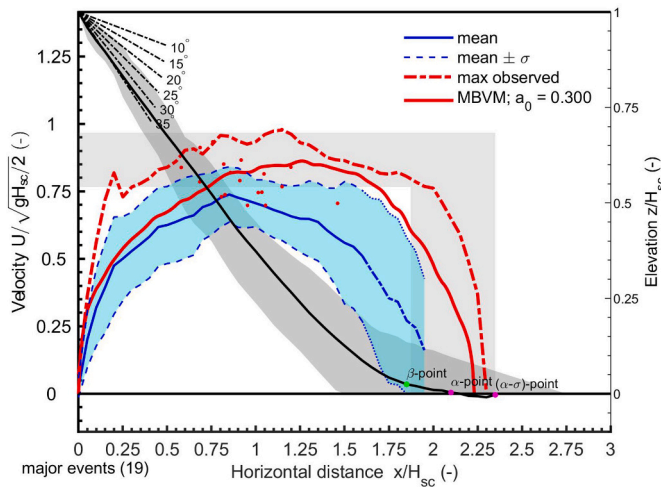

Fig. 8. Simulation (red solid line) along the "mean" path with $M_0 \approx 9.8 \cdot 10^4$ kg m^{-1} and $H_{SC} = 1000$ m. In addition, a summary of measured front-velocities from major avalanche events in various tracks are shown. The blue line shows the mean, the blue shaded area the $\pm \sigma$-range and the red dashed line the observed maximum derived from observations along the track. Red dots mark the maximum of the different measurements. The black line represents a "mean path" geometry and the gray shaded area the envelope of all path geometries. The light gray polygon gives an impression of the expected ranges for major avalanches according to the observations as presented in Fig. 1. The model parameters are given in Table 1.

4.5. Tamokdalen (NO), 2019-01-02

An avalanche accident, which took place on 2 January 2019 below Blåbærtinden, Tamokdalen in North Norway, provided a rare data set of GPS-data (for more information on the accident, see Sandersen, 2019). One victim was warring a wristwatch/heartbeat monitor with a tracking frequency of approximately 1/s as he was transported by the avalanche over a drop height of about 200 m. The GPS-data allowed an
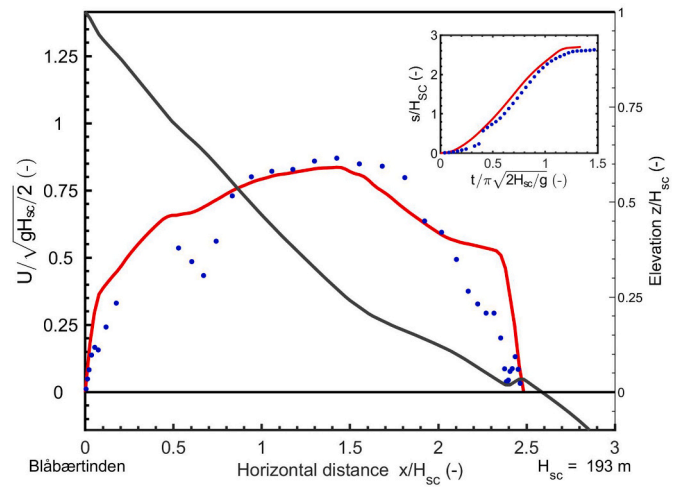

Fig. 9. Avalanche velocity as estimated by the model (red line) and as inferred from GPS records extracted from the wristwatch/heartbeat monitor of one of the victims (blue dots). Here $H_e = 0.25$ m, the remaining model parameters are given in Table 1. The inlet shows the corresponding s-t plot (distance and time are scaled).

estimate on the avalanche velocity during the descent of victim. Fig. 9 shows the comparison of the velocity estimates and a simulation with the "base" parameter in Table 1. The model provides again a good estimate for the event, both in respect to velocity and runout, even if a tip of the actual avalanche went slightly further.

4.6. Austria

The comparison between observed runout distances along the track, S_f, and simulations is shown in Fig. 10 for two combined data sets from Austria (Klenkhart and Weiler, 1994; Wagner, 2016). The events were all natural releases and thought to have rather high return periods in the order of $\mathcal{O}(100 \text{ years})$. No detailed velocity information are available. Out of the data set of 134 avalanches, 120 had sufficient geometry information (i.e., provided long enough profiles) for the comparison. The data cover a range of $H_{SC} \approx [110 \text{ m}, 1810 \text{ m}]$ and $\beta \approx [18°, 39°]$.

The maximum velocity for the simulations is $U/\sqrt{gH_{Se}/2} \sim 0.9$, where H_{Se} is the effective simulated drop height. In general, the model catches the observations rather well. The correlation between the modeled and observed runout distances is approximately 0.94 and the interquartile range of the relative error is 0.13. Nonetheless, there are several marked out-layers. In those cases a slight change in the parameters, which would also reflects the expected return period of the event better, may provide even lesser spreading. In some of these cases only a slight change in the parameters can cause a considerable change in the runout distance.

4.7. Aulta avalanche, Lukmanier (CH), 1984-02-08

How the various parameters influence the simulation results is shown in Fig. 11. The corresponding parameters are given in Table 2. For this comparison, the Aulta avalanche from 8 February 1984 (for details on the event, see Gubler et al., 1986; Gauer, 2013) is chosen as a complete velocity profile (solid black line) along the whole track exists and as it is a known event used in several publications.

The first simulation with the "base" parameters according to Table 1 (run 1) provides again a good estimate on the observations. Reducing the initial mass, M_0, causes a decrease in runout and velocity (run 2) because the retarding effect due to erosion increases (i.e. the ratio $\rho_s d_e / c_0 \rho_r D_{rel}$ in (23) increases). The same is observed for increasing the erosion depth H_e (run 3). Mass loss has likewise an important effect, both on the velocity and runout (run 4). As easily seen, decreasing the
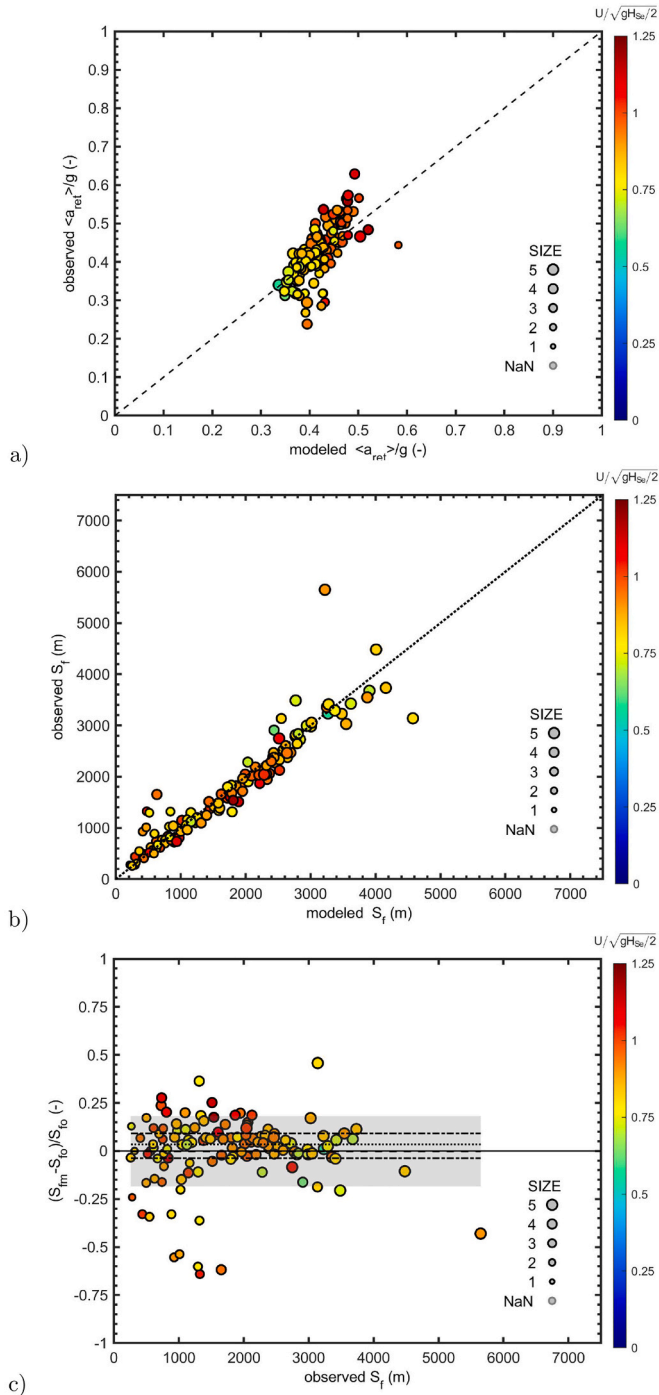
a)

b)

c)

Fig. 10. Simulations of the runout distances of two combined data sets from Austria. The model parameters are given in Table 1. a) mean retarding acceleration $<a_{ret}>/g = \Delta H/S_f$, where ΔH is the drop height between release area and runout; b) runout distance along the track S_f; and c) the relative error $(S_{fm} - S_{fo})/S_{fo}$, where S_{fo} marks the observations and S_{fm} the simulation. The dashed line shows the mean, the gray shaded area the corresponding standard deviation and the dash-dotted lines mark the interquartile range. The marker size indicates the avalanche size, if data are available. The scaled maximum velocity is color coded. The dotted lines in the two upper panels indicate a one-to-one relationship.

effective friction factor, a_0, will increase the velocity and runout (run 5). That some of the effects can compensate each other is shown by run 6, where decreasing the friction factor, a_0, compensates partly for the increase in erosion depth, H_e. Likewise run 7, where the increase in
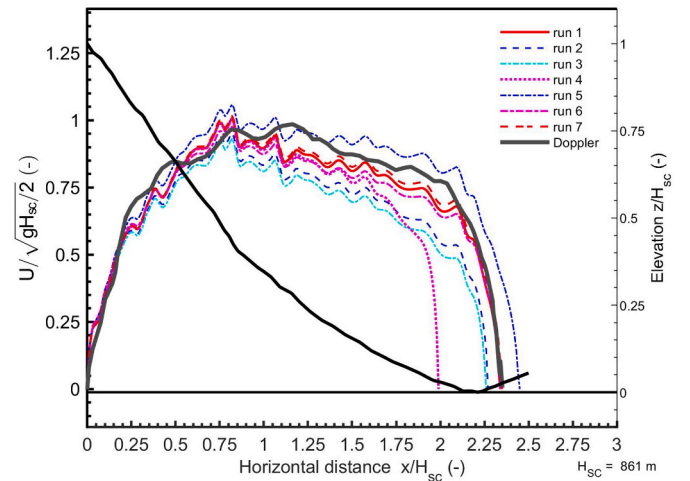

Fig. 11. Simulations of the Aulta avalanche 1984-02-08 (Lukmanier, Switzerland). Measurement by Gubler et al. (1986) with a CW Doppler-radar. The model parameters are given in Table 2.

Table 2
Parameter sets used for the Aulta avalanche simulations. Bold values mark the parameter changes.

run		1	2	3	4	5	6	7
M_0	$[10^4 \text{ kg m}^{-1}]$	7.5	**2.5**	7.5	7.5	7.5	7.5	**30**
H_e	[m]	0.1	0.1	**0.4**	0.1	0.1	**0.4**	**0.4**
d_d	[m]	0	0	0	**1.0**	0	0	0
a_0	[−]	0.3	0.3	0.3	0.3	**0.26**	**0.26**	0.3
μ_s	[−]	0.6	0.6	0.6	0.6	0.6	0.6	0.6
ρ_s	$[\text{kg m}^{-3}]$	150	150	150	150	150	150	150
ρ_a	$[\text{kg m}^{-3}]$	150	150	150	150	150	150	150

initial mass, M_0, compensates for the increased erosion depth. However, the required increase of initial mass is considerable in this case. This can be seen from Eq. (23). By keeping all parameters the same, except of the erosion depth, d_e, and the fracture depth, D_{rel}, the ratio d_e/D_{rel} should stay approximately the same to reach similar maximum velocities.

4.8. Sensitivity test

Fig. 13 shows a Monte-Carlo simulation for the horizontally extended "mean track" in Fig. 8. The parameter distributions used are shown in Fig. 12. They are based on observations or best guesses. Relying upon observations by Perla (1977) (see also Fig. 3), the critical snow depth, HS_0, is assumed to follow a half-normal distribution with a mean of approximately 1.4 m and a standard deviation of 0.6 m. The entrainment depth is given by a lognormal distribution with a mean of approximately 0.5 m and a standard deviation of 0.6 m. Using data by van Herwijnen and Heierli (2009) and Simenhois et al. (2012), μ_s is approximated by a general extreme value distribution with a shape parameter, $k_{gev} \approx 0.29$, scale parameter, $\sigma_{gev} \approx 0.036$, and location parameter $\mu_{gev} \approx 0.567$. The remaining parameters are taken as normal distributed with $\rho_s = N(150,15)$, $\rho_a = N(150,15)$, and $a_0 = N(0.3,0.015)$ ($a_0 = N(0.33,0.015)$ for the case of Ryggfonn in Fig. 14).

Comparing the range of observations in Fig. 8 with the model results in Fig. 13 suggests that the model gives reasonable first estimates for those major avalanches, covering more or less the full range.

Fig. 14 shows a similar Monte Carlo simulation for the Ryggfonn path. The same parameters are used as before, except d_{d0} in Eq. (29) is given by a uniform distribution with a mean of 1 m and for μ_d a normal distribution is used where $\mu_d = \max(0, N(0.26, 0.052))$. This will allow for actual mass loss and accounts to a degree for the spread in relative
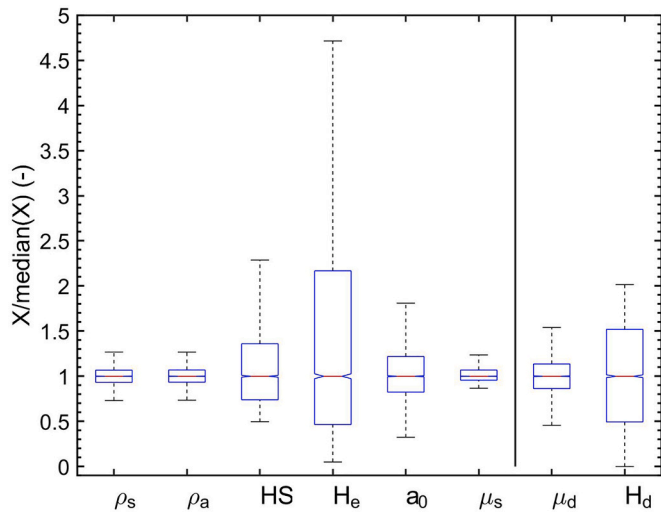
Fig. 12. Parameter distributions used in the Monte Carlo simulations. Values on the right of the vertical line are used additionally in the simulations for Ryggfonn. Values are normalized by their respective median: $\rho_s = 150$ kg m^{-3}; $\rho_a = 150$ kg m^{-3}; $HS \approx 1.3$ m; $H_e \approx 0.25$ m; $a_0 = 0.3/0.33$; $\mu_s = 0.58$; $\mu_d = 0.26$; $d_{d0} \approx 1$ m.
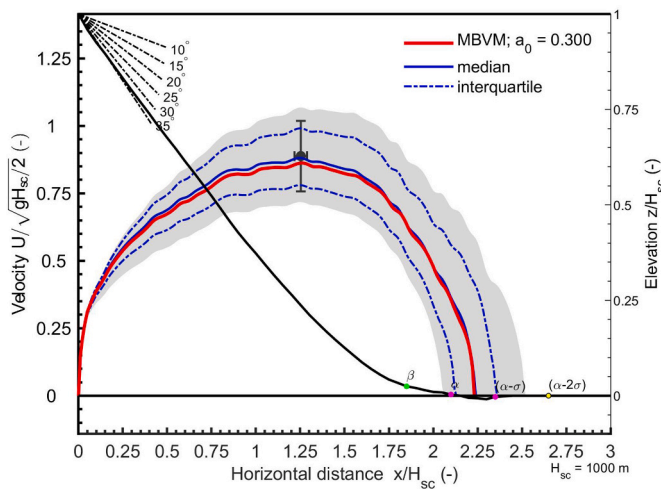

Fig. 13. Monte Carlo simulation (median; solid blue line). The test is run for a horizontally extended "mean" path shown in Fig. 8. The parameter distributions used are shown in Fig. 12. The remaining parameters are given in Table 1. The light gray polygon gives an impression of the inter-quantile-range 0.1–0.9 and the blue dashed lines of the interquartile range. The errorbar depicts the mean of the simulated maximum velocity and its position. For comparison, the red line shows the simulation with the "base" parameter given in Table 1 and shown in Fig. 8.

Fig. 14. Monte Carlo simulation (median; solid blue line). The test is run for the Ryggfonn path shown in Fig. 7. The parameter distributions used are shown in Fig. 12. The remaining parameters are given in Table 1. The light gray polygon gives an impression of the inter-quantile-range 0.1–0.9 and the blue dashed lines of the interquartile range. The errorbars depict the mean and interquartile range of the simulations of the velocity taken between positions of load plates LC54 and LC321 and the velocity at the base of the catching dam. For comparison, the red line shows the simulation with the "base" parameter given in Table 1. The red dashed line redraws the run with adapted parameters shown in Fig. 7.

Fig. 15. Comparison between runout observations and Monte Carlo simulations with and without dam. For the comparison only those simulations are considered that surpassed transmission line (SC123).

size and ambient conditions of the events shown in Fig. 7. In our case, deposition accounts to large degree for that the avalanche stops even in steeper parts of the slope, which can often be observed in nature. The effect was already seen in Fig. 11 run 4. Also in the present case, the model shows a decent overall match compared to the observations in Fig. 7.

Fig. 15 compares the comparative cumulative distribution functions (CCDF; probability of exceedance) of the observed runouts at Ryggfonn (for more deatils on the data see Gauer and Kristensen, 2016; Gauer et al., 2009) and corresponding ones of Monte Carlo simulations with (see Fig. 14) and without catching dam. To be consistent with the observations, for the comparison, only those avalanches are considered that reached the runout area (i.e. surpassed at least the elevation of the former transmission line marked as SC123). Considering the simple
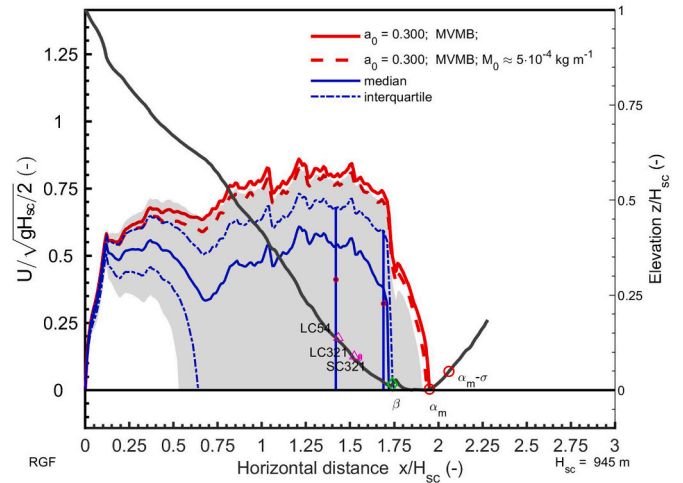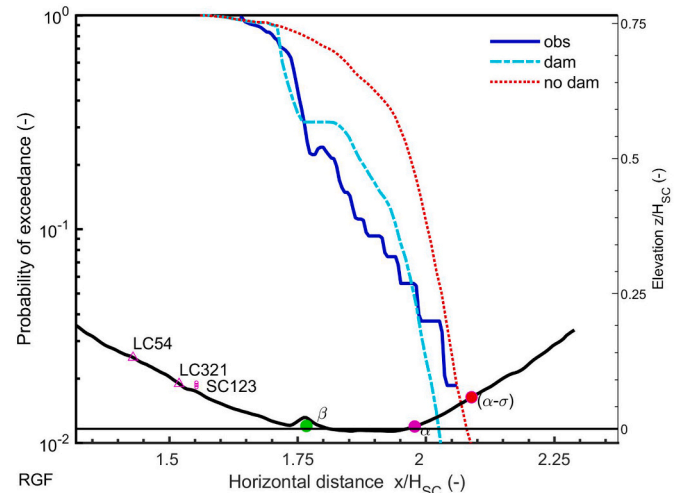
approach of the mass block model and the uncertainties involved in the measurements and their reporting (e.g., avalanche type; the distinction between the deposits of the dense or fluidized part and those of the powder part; or the degree of pre-filling of the catching dam), the model provides reasonable estimates on the avalanche runouts.

5. Concluding remarks

This paper presents a simple mass block model that includes basic observations of major dry-mixed avalanches, such as mass entrainment and deposition and is basically scale invariant to the total drop height. All its parameters, except of the effective friction parameter, a_0, are more or less observable in the field. For the effective friction parameter, a_0, we take granular flow as guidance and use a value that is consistent with chute experiments using dry snow (e.g. Platzer et al., 2007).

Although it is only simple a mass block model, it is still an admissible first-order approximation. The model is dominated by a Coulomb like friction, which is in line with results, e.g., by Ancey and Meunier (2004); Ancey (2005). Mass erosion, however, causes an apparent velocity squared dependency. This dependency is governed by the ratio between entrained mass per unit area and the (initial) avalanche mass. A relatively large initial mass or little entrainment will favor slightly faster avalanches with longer runouts, which is quite in accordance with observations. In contrast to, e.g., Voellmy-type models or the NIS-model, the model parameters for the presented model are invariant to drop height.

Despite all the uncertainties associated with the model and the observations shown, the model provides reasonable results for major events as demonstrated above. The simulations demonstrate clearly that besides mass entrainment, mass loss can have a significant influence on the runout and velocity of avalanches. The obvious influence of mass erosion puts limits to the meaningfulness of granular experiments that neglect erosion. This holds also true for numerical models that do not include erosion and deposition. To improve the verification of the model approach, more combined observations on velocity, runout distances, mass balance, and snowpack properties from various observation sites that show different geometries (e.g., mean slope angles and drop heights) are desirable.

At present, we use a rather simple approach for the entrainment and loss of mass in the model. For the mass block model this is reasonable, especially the entrainment model. More sophisticated 2-D (or even 3-D) models will require more enhanced models for entrainment and mass deposition, models like the ones by Rauter and Köhler (2019); Naaim et al. (2004).

The effective friction parameter, a_0, probably depends on the state of flow and may vary to a certain degree along the track, which needs to be accounted for. In our Monte Carlo simulations, we assumed that all parameter distributions are independent, however, some of the parameters might be correlated.

The presented model can be a useful simple tool for practitioners, especially in combination with Monte Carlo simulations, to obtain first estimates on runout distances of major avalanches as required in hazard mapping. The model circumvents the problem of finding a suitable β-point (for a discussion on the issue see, e.g. Sinickas and Jamieson, 2014), which is necessary for the known statistical runout models, like the $\alpha - \beta$ model (Lied and Bakkehøi, 1980) or the run-out ratio model (McClung and Mears, 1991). At the same time, the model provides also speed estimates. As several input parameters are observable in the field, the model can be adapted to local conditions. Following the approach by Nohguchi (1989), it can easily be extended into a three dimensional space. This can reduce the uncertainty due to subjectively drawing profile lines. Furthermore, the model allows to include other resistance terms, e.g., the effect of forest to a certain degree. The latter, may require estimates on the flow height, which mass block models can principally not provide.

Author statement

The paper was solely written by the author.

Declaration of Competing Interest

The author declares that he has no known competing financial interests or personal relationships that could have appeared to influence the work reported in this paper.

Acknowledgments

References

Ancey, C., 2005. Monte Carlo calibration of avalanches described as Coulomb fluid flows. Philos. Trans. R. Soc. A-Mathematical Phys. Eng. Sci. 363, 1529–1550. https://doi.org/10.1098/rsta.2005.1593.

Ancey, C., Meunier, M., 2004. Estimating bulk rheological properties of flowing snow avalanches from field data. J. Geophys. Res. Earth Surf. 109, F01004 (1–15). https://doi.org/10.1029/2003JF000036.

Bazant, Z.P., Zi, G., McClung, D., 2003. Size effect law and fracture mechanics of the triggering of dry snow slab avalanches. J. Geophys. Res. Solid Earth 108, 2119. https://doi.org/10.1029/2002JB001884.

Cherepanov, G.P., 2019. Snow avalanches, in: Invariant Integrals in Physics. Springer International Publishing, pp. 197–214. https://doi.org/10.1007/978-3-030-28337-7_9.

Cherepanov, G.P., Esparragoza, I.E., 2008. A fracture-entrainment model for snow avalanches. J. Glaciol. 54, 182–188. https://doi.org/10.3189/002214308784409071.

Coaz, J.W.F., 1910. Statistik und Verbau der Lawinen in den Schweizeralpen. Bern, Stämpfli & Cie. Etc. With plates and maps.

Curcic, M., Haus, B.K., 2020. Revised estimates of ocean surface drag in strong winds. Geophys. Res. Lett. 47. https://doi.org/10.1029/2020GL087647.

Faillettaz, J., Louchet, F., Grasso, J., 2006. Cellular automaton modelling of slab avalanche triggering mechanisms: from the universal statistical behaviour to particular cases. In: Proceedings of the 2006 International Snow Science Workshop, Telluride, Colorado, pp. 174–180.

Gauer, P., 2013. Comparison of avalanche front velocity measurements: supplementary energy considerations. Cold Reg. Sci. Technol. 96, 17–22. https://doi.org/10.1016/j.coldregions.2013.09.004.

Gauer, P., 2014. Comparison of avalanche front velocity measurements and implications for avalanche models. Cold Reg. Sci. Technol. 97, 132–150. https://doi.org/10.1016/j.coldregions.2013.09.010.

Gauer, P., 2016. Selected observations from avalanche measurements at the Ryggfonn test site and comparisons with observations from other locations. In: Proceedings of the International Snow Science Workshop 2016, Breckenrigde, CO, pp. 1340–1347.

Gauer, P., 2018a. Avalanche probability: Slab release and the effect of forest cover. In: Proceedings of the International Snow Science Workshop 2018, Innsbruck, Austria, pp. 76–83.

Gauer, P., 2018b. Considerations on scaling behavior in avalanche flow along cycloidal and parabolic tracks. Cold Reg. Sci. Technol. 151, 34–46. https://doi.org/10.1016/j.coldregions.2018.02.012.

Gauer, P., Issler, D., 2004. Possible erosion mechanisms in snow avalanches. Ann. Glaciol. 38, 384–392. https://doi.org/10.3189/172756404781815068.

Gauer, P., Kristensen, K., 2016. Four decades of observations from NGI's full-scale avalanche test site Ryggfonn—summary of experimental results. Cold Reg. Sci. Technol. 125, 162–176. https://doi.org/10.1016/j.coldregions.2016.02.009.

Gauer, P., Lied, K., Kristensen, K., 2008. On avalanche measurements at the Norwegian full-scale test-site Ryggfonn. Cold Reg. Sci. Technol. 51, 138–155. https://doi.org/10.1016/j.coldregions.2007.05.005.

Gauer, P., Lied, K., Kristensen, K., 2009. Analysis of avalanche measurements out of the runout area of NGI's full-scale test-site Ryggfonn. Cold Reg. Sci. Technol. 57, 1–6. https://doi.org/10.1016/j.coldregions.2008.12.005.

Gauer, P., Kronholm, K., Lied, K., Kristensen, K., Bakkehøi, S., 2010. Can we learn more from the data underlying the statistical α-β model with respect to the dynamical behavior of avalanches? Cold Reg. Sci. Technol. 62, 42–54. https://doi.org/10.1016/j.coldregions.2010.02.001.

Gaume, J., Chambon, G., Eckert, N., Naaim, M., 2012. Relative influence of mechanical and meteorological factors on avalanche release depth distributions: an application to French Alps. Geophys. Res. Lett. 39, L12401. https://doi.org/10.1029/2012GL051917.

Greene, E., Atkins, D., Birkeland, K., Elder, K., Landry, C., Lazar, B., McCammon, I., Moore, M., Sharaf, D., Sternenz, C., Tremper, B., Williams, K., 2016. Snow, Weather, and Avalanches: Observation Guidelines for Avalanche Programs in the United States. Technical Report. American Avalanche Association.

Gubler, H.U., Hiller, M., Klausegger, G., Suter, U., 1986. Messungen an Fliesslawinen. Zwischenbericht. Internal report 41. Swiss Federal Institute for Snow and Avalanche Research.

Heimgartner, M., 1977. On the flow of avalanching snow. J. Glaciol. 19, 357–363. https://doi.org/10.1017/S0022143000029385.

van Herwijnen, A., Heierli, J., 2009. Measurement of crack-face friction in collapsed weak snow layers. Geophys. Res. Lett. 36, L23502. https://doi.org/10.1029/2009GL040389.

Hetu, B., Brown, K., Germain, D., 2011. Fatal avalanche accidents in Quebec (Canada) 1825 to 2009. Canadian Geographer-Geographe Canadien 56, 273–287. https://doi.org/10.1111/j.1541-0064.2010.00338.x.

Issler, D., Jonson, A., Gauer, P., Domaas, U., 2016. Vulnerability of Houses and Persons under Avalanche Impact — The Avalanche at Longyearbyen on 2015-12-19, in: Proceedings of the International Snow Science Workshop 2016, Breckenrigde, CO. pp. 371–378.

Klenkhart, C., Weiler, C., 1994. Lawinen Technische Aufnahmen in den Bundesländern Vorarlberg, Tirol, Kärnten, und Salzburg. Technical Report. Forsttechnischer Dienst für Wildbach und Lawinenverbauungen, Sektion Tirol, Innsbruck.

Lang, T.E., Dent, J.D., 1982. Review of surface friction, surface resistance, and flow of snow. Rev. Geophys. Space Phys. 20, 1. https://doi.org/10.1029/RG020i001p00021.

Lied, K., Bakkehøi, S., 1980. Empirical calculations of snow-avalanche run-out distance based on topographic parameters. J. Glaciol. 26, 165–177. https://doi.org/10.1017/S0022143000010704.

McClung, D.M., 2003. Size scaling for dry snow slab release. J. Geophys. Res. 108, 2465. https://doi.org/10.1029/2002JB002298.

McClung, D.M., 2009. Dimensions of dry snow slab avalanches from field measurements. J. Geophys. Res. Earth Surf. 114, F01006. https://doi.org/10.1029/2007JF000941.

McClung, D.M., Gauer, P., 2018. Maximum frontal speeds, alpha angles and deposit volumes of flowing snow avalanches. Cold Reg. Sci. Technol. 153, 78–85. https://doi.org/10.1016/j.coldregions.2018.04.009.

McClung, D.M., Mears, A.I., 1991. Extreme value prediction of snow avalanche runout. Cold Reg. Sci. Technol. 19, 163–175. https://doi.org/10.1016/0165-232X(91)90006-3.

McClung, D., Schaerer, P., 2006. The Avalanche Handbook. 3rd ed., the Mountaineers Books, 1011 SW Klickitat Way, Seattle, Washington 98134.

Naaim, M., Naaim-Bouvet, F., Faug, T., Bouchet, A., 2004. Dense snow avalanche modeling: flow, erosion, deposition and obstacle effects. Cold Reg. Sci. Technol. 39, 193–204. https://doi.org/10.1016/j.coldregions.2004.07.001.

Nohguchi, Y., 1989. Three-dimensional equations for mass centre motion of an avalanche of arbitrary configuration. Ann. Glaciol. 13, 215–217. https://doi.org/10.1017/S0260305500007928.

Norem, H., Irgens, F., Schieldrop, B., 1987. A continuum model for calculating snow avalanche velocities. In: Salm, B., Gubler, H. (Eds.), Avalanche Formation, Movements and Effects. Proceedings of the Davos Symposium, September 1986. 162. IAHS Press, Inst. of Hydrology, Wallingford, Oxfordshire, pp. 363–380 OX10 8BB, UK.

Perla, R., 1977. Slab avalanche measurements. Can. Geotech. J. 14, 206–213. https://doi.org/10.1139/t77-021.

Perla, R., Cheng, T.T., McClung, D.M., 1980. A two-parameter model of snow-avalanche motion. J. Glaciol. 26, 119–207. https://doi.org/10.1017/S002214300001073X.

Platzer, K., Bartelt, P., Jaedicke, C., 2007. Basal shear and normal stresses of dry and wet snow avalanches after a slope deviation. Cold Reg. Sci. Technol. 49, 11–25. https://doi.org/10.1016/j.coldregions.2007.04.003.

Rauter, M., Köhler, A., 2019. Constraints on entrainment and deposition models in avalanche simulations from high-resolution radar data. Geosciences 10, 9. https://doi.org/10.3390/geosciences10010009.

Rosenthal, W., Elder, K., 2003. Evidence of chaos in slab avalanching. Cold Reg. Sci. Technol. 37, 243–253. https://doi.org/10.1016/S0165-232X(03)00068-5.

Sandersen, F., 2019. Snøskredulykke i Tamokdalen 2019-01-02 / Snow Avalanche Accident in the Tamok Valley, 2019-01-02. Techreport 20170131-13-TN rev1. Norwegian Geotechnical Institute (In Norwegian with English summary).

Savage, S., Hutter, K., 1989. The motion of a finite mass of granular material down a rough incline. J. Fluid Mech. 199, 177–215. https://doi.org/10.1017/S0022112089000340. copy.

Schweizer, J., Michot, G., Kirchner, H.O.K., 2004. On the fracture toughness of snow. Ann. Glaciol. 38, 1–8. https://doi.org/10.3189/172756404781814906.

Simenhois, R., Birkeland, K.W., van Herwijnen, A., 2012. Measurements of ECT Scores and Crack-Face Friction in Non-persistent Weak Layers: What Are the Implications for Practitioners?, in: Proceedings, 2012 International Snow Science Workshop, Anchorage, Alaska. pp. 104–110.

Sinickas, A., Jamieson, B., 2014. Comparing methods for estimating β points for use in statistical snow avalanche runout models. Cold Reg. Sci. Technol. 104-105, 23–32. https://doi.org/10.1016/j.coldregions.2014.04.004.

Sovilla, B., 2004. Field experiments and numerical modelling of mass entrainment and deposition processes in snow avalanches. Diss. ETH no. 15462. ETH Zurich. Zurich, Switzerland. https://doi.org/10.3929/ethz-a-004784844.

Sovilla, B., Burlando, P., Bartelt, P., 2006. Field experiments and numerical modeling of mass entrainment in snow avalanches. J. Geophys. Res. Earth Surf. 111https://doi.org/10.1029/2005JF000391. F03007(1–16).

Sovilla, B., McElwaine, J.N., Schaer, M., Vallet, J., 2010. Variation of deposition depth with slope angle in snow avalanches: Measurements from Vallée de la Sionne. J. Geophys. Res. Earth Surf. 115, F02016 (1–13). https://doi.org/10.1029/2009JF001390.

Voellmy, A., 1964. On the destructive force of avalanches (translation by R. E. Tate). Translation 2. Alta Avalanche Study Center Wasatch National Forest. Translate by R. E. Tata.

Wagner, P., 2016. Kalibrierung des α-β-Modells für das Ermitteln der Auslauflänge von kleinen und mittleren Lawinen. Master thesis. Institut für Alpine Naturgefahren (IAN). BOKU-Universität für Bodenkultur.